

<https://doi.org/10.1038/s43247-024-01402-x>

# Video-based measurements of the entrainment, speed and mass flux in a wind-blown eruption column

Check for updates

Nicola Mingotti &amp; Andrew W. Woods

On May 4 2010 a wind-blown ash plume issued from Eyjafjallajökull volcano in Iceland. Analysis of a 17-minute-long video recording of the eruption suggests that, within 2–2.5 km of the vent, the flow was moving with the wind and rising under buoyancy, following a trajectory directly analogous with laboratory experiments of turbulent buoyant plumes in a cross-flow. The radius of the time-averaged ash cloud grew with height  $z$  at a rate  $r = 0.48z$ , corresponding to an entrainment coefficient 0.4, again consistent with laboratory experiments. By analysing the frames in the video and comparing the shape of the plume to that predicted by the model, we estimate that during the 17 minutes recorded, the eruption rate gradually decreased by about 43% from an initial rate of  $1.11 \times 10^4 \text{ kg s}^{-1}$  to  $0.63 \times 10^4 \text{ kg s}^{-1}$ . The analysis reported herein opens the way to assess eruption rates and eruption column processes from video recordings during explosive volcanic eruptions.

The dynamics of volcanic eruption columns involve the two-phase interaction of hot fragmented ash and pumice with volcanic gases and entrained air. There has been a very substantial literature about the dynamics of these plumes over the past 30 years<sup>1–3</sup> following the classical work on turbulent buoyant plumes<sup>4</sup>. There has also been progress modelling the effects of ambient wind, which can dominate the dynamics of smaller eruption columns<sup>5–7</sup>.

Typically, models of eruption columns are based on conservation laws for the plume properties integrated across the area of the plume. The entrainment of air into the plume is a critical process controlling the dynamics: it is often quantified in terms of an entrainment constant  $\alpha$  multiplied by the plume and wind speed, with the entrainment constant increasing by a factor of 4–5 if the plume evolves from being near vertical at the source to more strongly wind-blown downstream<sup>8–11</sup>, but it is difficult to measure this directly from field observations.

Many models for wind-blown plumes have adopted the so-called Lagrangian approach of modelling, in which the evolution of the plume is described along the axis of the plume following the original models of Hoult et al.<sup>12</sup> and Hewett et al.<sup>13</sup>. The height of rise of actual eruption columns have been related to the eruption properties and prevailing winds, thereby providing some constraints for these models<sup>7,9,11</sup>.

However, there are relatively few detailed observations of the shape and turbulent properties of wind-blown volcanic plumes as a function of height and time with which models can be compared. Very fortunately, we have been provided with a 17 min, high-resolution movie (1440 × 810 pixels, 25

frames per second) of the plume from the May 4th 2010 eruption of the Eyjafjallajökull Volcano by Costanza Bonadonna of Geneva University. Some of the data in this movie was originally described in the paper by Manzella et al.<sup>14</sup>; in particular, Manzella et al. observed fingers of relatively dense, particle-laden air descending underneath the plume and measured the speed of descent of these structures. By collecting samples of the deposit on the ground after the end of the eruption, they showed that the finger descent speed correlates with the fall speed of the particles.

Here we report some new image processing results of this movie which identify: (i) the length scale over which the horizontal plume speed adjusts to the ambient wind speed; and (ii) the evolution of the time average and fluctuations of the radius and centre of mass of the plume as it moves downwind. This provides new constraints on the entrainment rate into plumes dominated by the wind, and we find these are consistent with laboratory experiments. Using a simplified theoretical model in conjunction with the data, we estimate that during this 17 minute eruption sequence, the eruption rate gradually decreased by about 43%.

## Results

### Adjustment of the downwind plume speed to the wind speed

We first explore the relation between the wind speed and the lateral speed of the plume. In the frame of the video, wind blows from left to right and so the plume is transported towards the right hand side of the frame while rising. On the day of the eruption, the weather was clear, but traces of mist and water vapour are visible against the blue sky background on the left hand

Institute for Energy and Environmental Flows, University of Cambridge, Madingley Road, Cambridge CB3 0EZ, UK.

 e-mail: [aww1@cam.ac.uk](mailto:aww1@cam.ac.uk)

side of (Fig. 1a): these white vapour clouds appear to be advected by the wind over time. (Fig. 1b) shows a time series of a horizontal row of pixels, which is denoted by a dotted line in panel (a), and which is located at a height  $z \approx 850$  m above the vent. On the left hand side of this time series image, we observe a number of inclined fronts (see black arrow in Fig. 1b). By analysing the red, blue and green colour channels in the video, we have found that these fronts exhibit very different levels of saturation in the blue channel. These fronts illustrate the motion of the vapour clouds being advected by the wind. Using the Hough transform algorithm as available in Matlab, we can

identify these fronts and calculate their gradient to estimate the mean advection speed,  $w$ . While speed measurement based on the Hough transform has relatively small errors of just a few percent<sup>15</sup>, there is some uncertainty associated with the height of the clouds relative to the location where the video was recorded. However, measurements of several clouds over this 17 min video provide very consistent results, with advection speeds of order  $8\text{--}10\text{ m s}^{-1}$  and limited vertical shear, as depicted in (Fig. 1c) (red diamonds). These results are consistent with, if somewhat smaller than, the field observation reported by Manzella et al.<sup>14</sup>, who measured wind speeds of

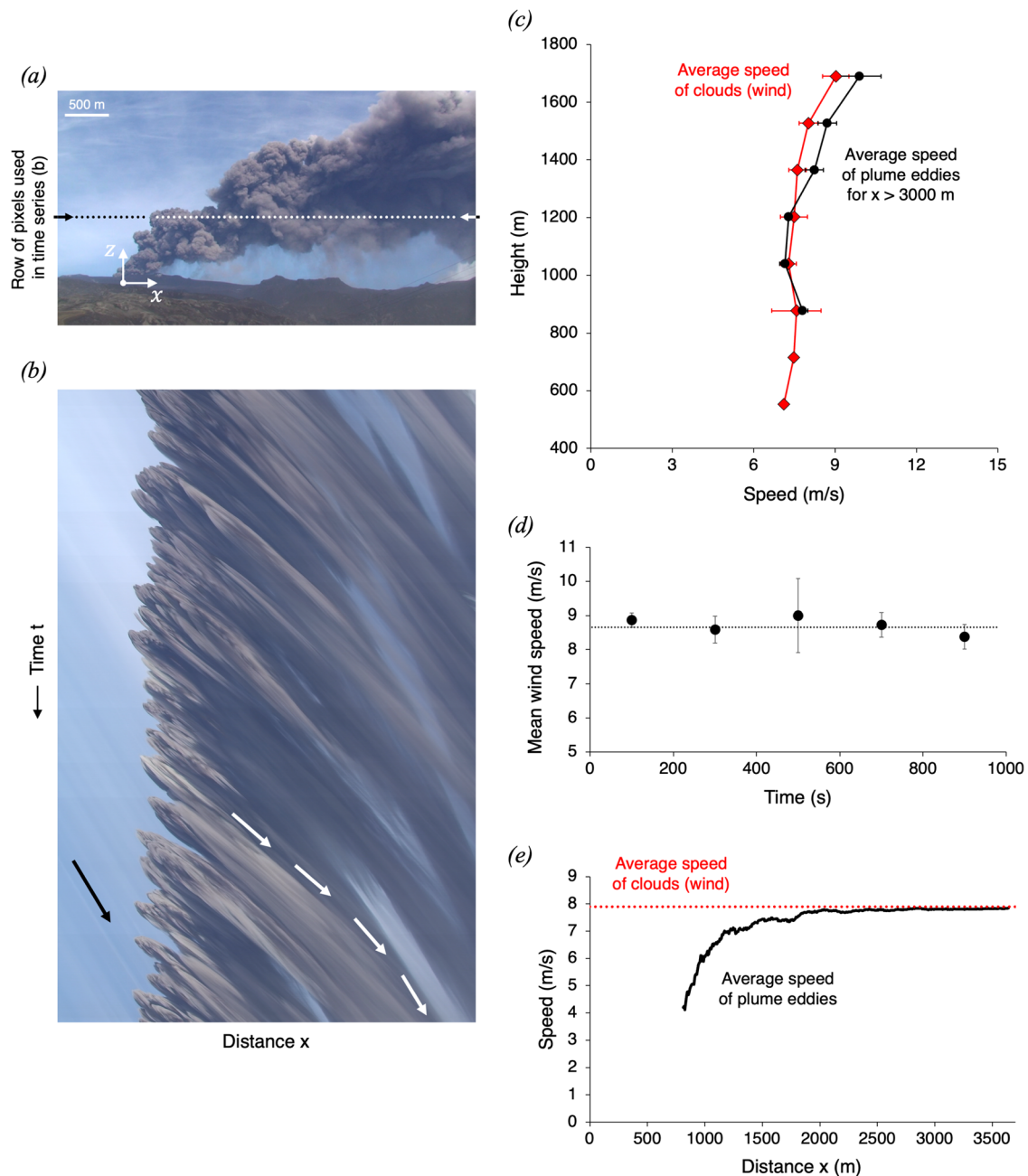
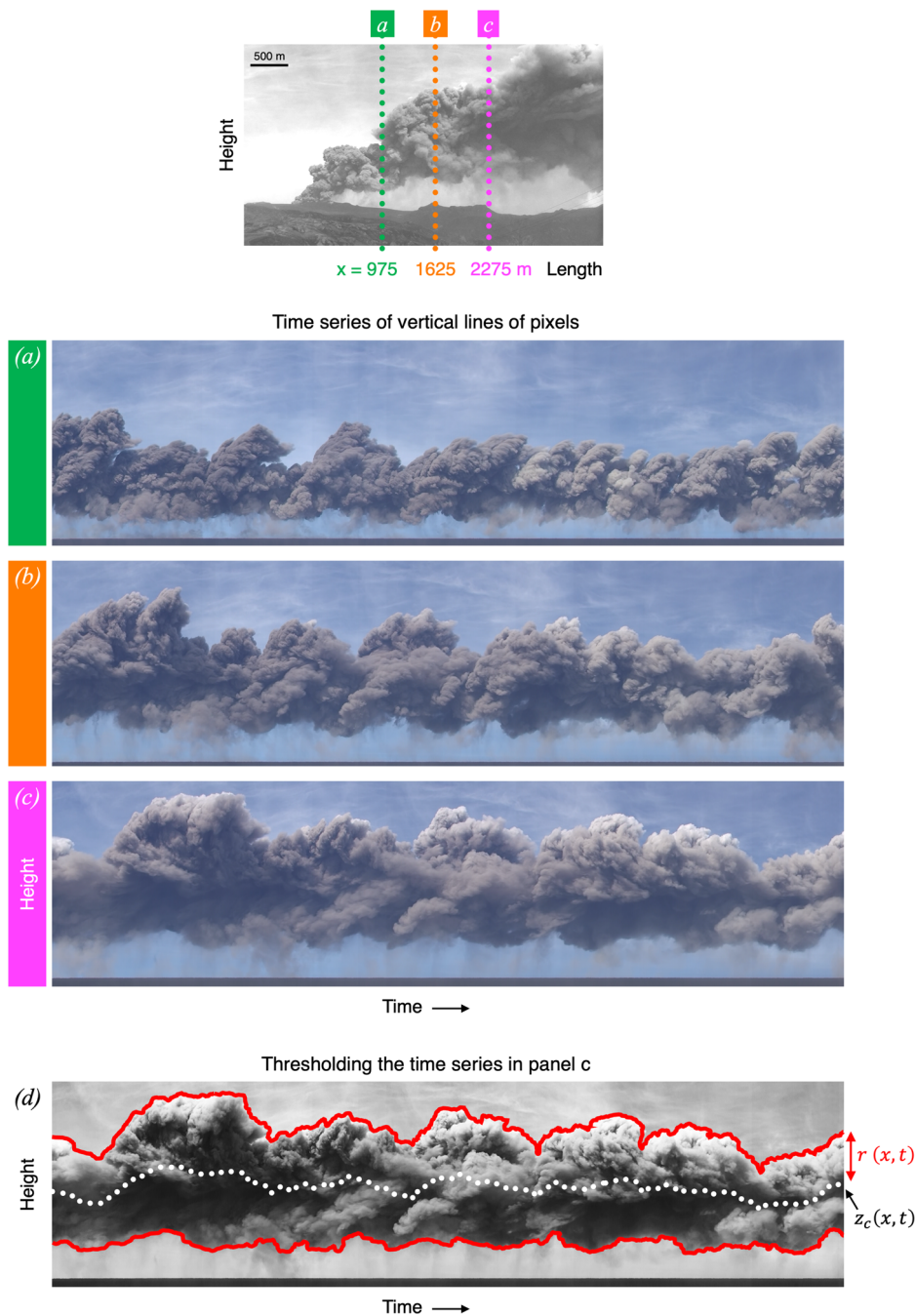


**Fig. 1 | Video-based measurement of the speed of the wind and of the ash plume.** **a** Photograph of the ash plume captured during the eruption. **b** Time series of the horizontal row of pixels marked by the dotted line in (a). On the left hand side of this time series image, we observe the trajectories in time of the white vapour clouds (see black arrow), which are visible against the blue sky background in (a). On the right hand side of the time series image, we observe the trajectories in time of the eddies in the plume (see white arrows). **c** Vertical profiles of the horizontal speed of the clouds/wind (red diamonds) and of the eddies in the plume, in the region  $x > 3000$  m (black

dots). **d** The vertically-averaged mean speed of the clouds/wind is approximately constant during the 17 min recorded. The error bars illustrate the standard deviation of the velocity measurements relative to the mean. **e** The black solid line illustrates the time-averaged horizontal speed of eddies in the plume, plotted as a function of downwind distance from the source, as measured at a height  $z \approx 850$  m above the vent. At large distances from the vent,  $x > 2500$  m, this speed approximates the background speed of the clouds at the same height  $z \approx 850$  m (red dotted line), which we assume to be close to the wind speed.

**Fig. 2 | Measurement of the height and radius of the volcanic plume as a function of time and distance from the vent.** Time series of three columns of pixels, located at different downwind distances in the plume: (a)  $x \approx 975$  m, (b)  $x \approx 1625$  m and (c)  $x \approx 2275$  m. **d** The time series image in (c) is thresholded in order to identify the edges of the ash cloud (red lines). The instantaneous centre of the cloud,  $z_c(x, t)$ , is defined as the locus of points which are equidistant from the edges (white dotted line), while the instantaneous radius of the cloud,  $r(x, t)$ , is the distance between the cloud centre and either edge.



$11.0 \pm 0.5 \text{ m s}^{-1}$  49 min before the eruption video was recorded. We have also checked whether the wind field changed in time during this video recording by analysing the speed of the wind over each fifth of the video, and we find that the speed is approximately constant in time (Fig. 1d).

The time series image in (Fig. 1b) also illustrates the motion of a series of eddy-type structures in the ash plume. The mean velocity of these structures varies with time and downwind distance from the source,  $x$ . Some of the spatial variation may be seen in the varying gradient of the white arrows in 1b.

The black solid line in (Fig. 1e) shows the time average of the horizontal speed of the eddies at a height of 850 m, as a function of the distance downstream. It is seen that at small distances from the source the horizontal component of the plume velocity is relatively small. At larger distances from the source, however, the plume speed increases, until for  $x > 2000\text{--}2500$  m, it becomes very similar to the background wind speed (red dotted line). (Fig. 1c) shows that the mean horizontal speed of the eddies (black dots)

approximates the wind speed (red diamonds) at sufficiently large distances from the source,  $x > 2500\text{--}3000$  m. This is consistent with a picture of the volcanic plume issuing vertically from the vent, but then rapidly adjusting to the wind speed in the downwind direction<sup>16</sup>.

### Variation of the plume radius and height with distance from the vent

We have also analysed the shape of the plume as a function of distance downstream. Figure 2 shows three time series of vertical lines of pixels located at different distances from the plume source: (a)  $x \approx 975$  m, (b)  $x \approx 1625$  m and (c)  $x \approx 2275$  m. A threshold in the blue channel has been applied to each image to identify the edges of the plume (red lines in Fig. 2d). Since the ash plume is opaque, it is difficult to estimate the concentration of the ash in the plume, and so the instantaneous centre of mass,  $z_c(x, t)$ , has been defined as the locus of points which are equidistant from the plume edges (white dotted line in Fig. 2d). The

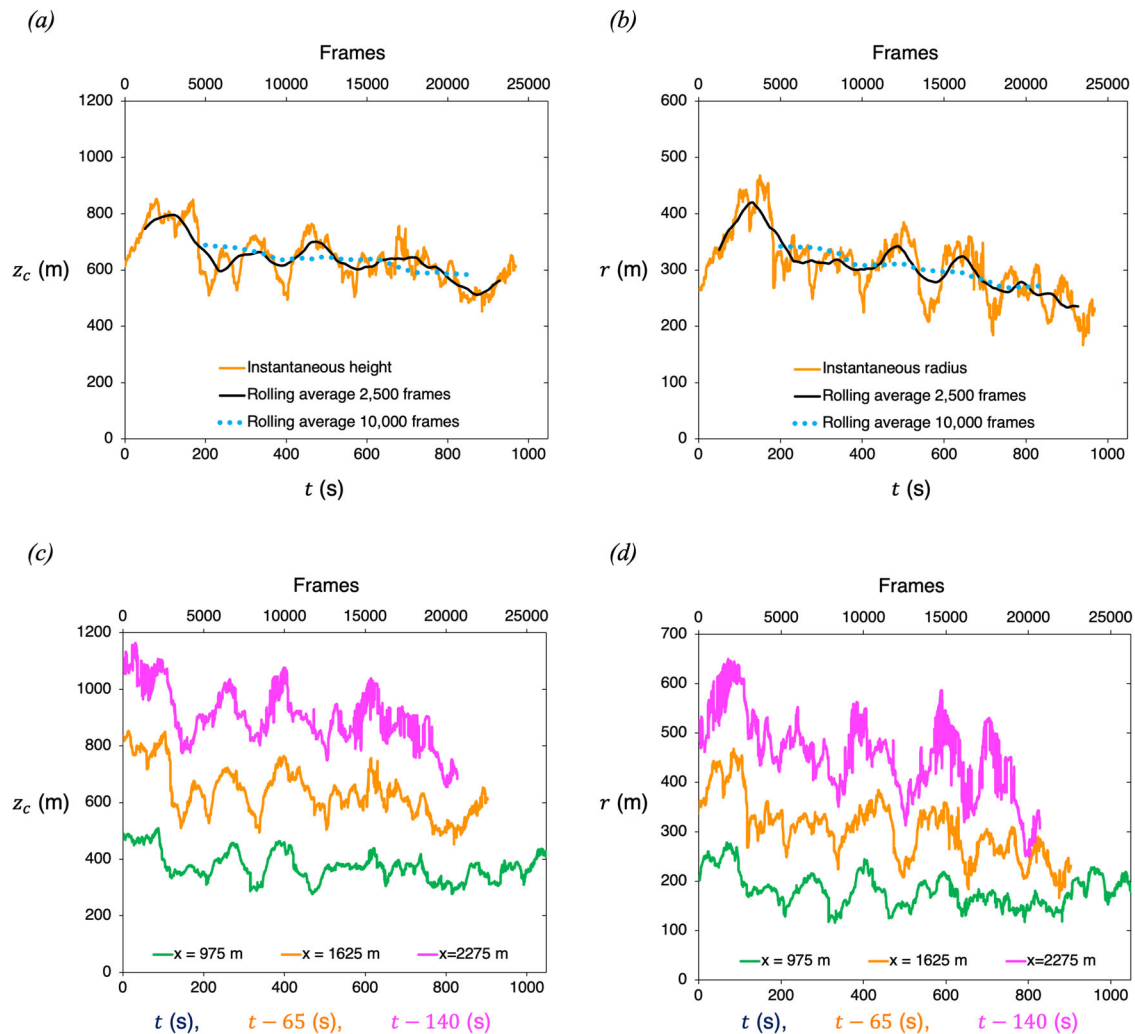


**Fig. 3 | Fluctuations in the plume height and radius over time.** In (a, b), we measure (a) the height  $z_c$  and (b) the radius  $r$  of the ash plume at a downwind distance  $x \approx 1625$  m from the source (see Fig. 2b), and plot the instantaneous values (orange lines), as well as the rolling averages produced by averaging over 2500 and 10,000 frames (black solid lines and blue dotted lines respectively). Panels (c, d)

illustrate the passage of eddies in the plume by comparing the instantaneous measurements of the height and radius at three downwind locations (lines are colour-coded as in Fig. 2). Virtual time origins are used on the horizontal axis, and the two downstream curves are moved forward by the amount of time required for the wind to flow from the upstream measurement position,  $\Delta t = \Delta x/w$ .

instantaneous radius of the plume,  $r(x, t)$ , has been defined as the distance between the centre of mass and either edge (Fig. 2d). Using these data, we have calculated the plume radius and centre of mass,  $r(x)$  and  $z_c(x)$  respectively, as a function of time, and these are shown in (Fig. 3a, b). The orange lines in these figures present the instantaneous data as measured a distance  $x = 1625$  m from the source (see Fig. 2b). We also plot rolling averages of the data, produced by averaging over 2500 and 10,000 frames (black solid line and blue dotted line respectively). For reference, the whole 17 min long movie contains about 26,200 frames.

The data show that the plume height and radius fluctuate in time and that, in addition, there is a steady decrease in the plume height and radius with time. In part the fluctuations are associated with the passage of eddies through the plume: these can be identified in (Fig. 3c, d), which compare the instantaneous measurements of the plume height and radius at the three locations depicted in Fig. 2. Given that the wind speed  $w$  is of order  $10 \text{ m s}^{-1}$ , eddies move across the field of view in about 300 s, corresponding to about 7500 frames. As a result, the shorter rolling time average still preserves information about eddies (black solid lines in Fig. 3a, b). The longer time average, however, smooths out this information and captures the longer-term trend, which suggests a gradual waning of the eruption (blue dotted lines in Fig. 3a, b). The ratio of the plume radius to the plume centreline height lies in the range  $0.46 < r/z_c < 0.50$ , with a mean value of 0.48, as seen in

the plot of radius vs. centreline height at each of these three positions downwind (Fig. 4a).

To assess whether the ratio  $r/z_c$  varies with time as a result of a change in the intensity of the eruption, we have then analysed each frame in the movie, and calculated the mean value of  $r/z_c$  averaged over the entire length of the plume. This is illustrated in (Fig. 4b) as a function of time. It is seen that, while there are some fluctuations in  $r/z_c$  over time, these are relatively small, and the ratio of the plume radius vs. centreline height remains in the range  $0.45 < r/z_c < 0.50$  during the whole movie, irrespective of any changes in the intensity of the eruption.

### Comparison with a time-averaged model for a wind-blown plume: Plume radius and entrainment coefficient

To assess whether the classical model for wind-blown plumes describes this volcanic ash plume, we first consider the entrainment coefficient. In the previous section, we found that the ratio of the plume radius to the height of the centreline (equation (3)) has value  $\alpha = 0.48 \pm 0.02$ , as may be seen from (Fig. 4a) and the solid black line in (Fig. 5c).

James et al.<sup>16</sup> carried out a similar analysis for a series of laboratory experiments in which saline water issued from a steadily moving source to generate a current-blown plume. They worked with the time-averaged dye concentration at each point in the plume (Fig. 5b), and found that the



**Fig. 4 | Ratio between the radius and the height of the volcanic plume.** **a** Cross-plot of the plume height vs. radius as measured at the three downwind distances from the source depicted in (Figs. 2, 3). **b** For each frame captured during the movie, we estimate the mean value of  $r/z_c$  along the plume, and plot this ratio as a function of time.

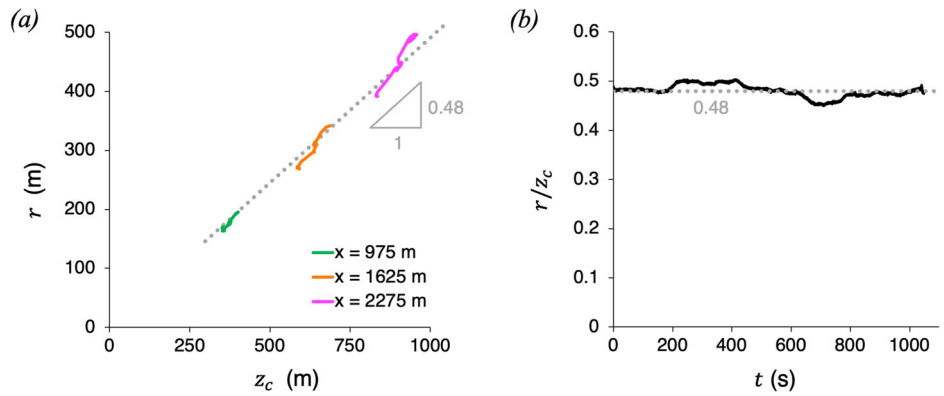
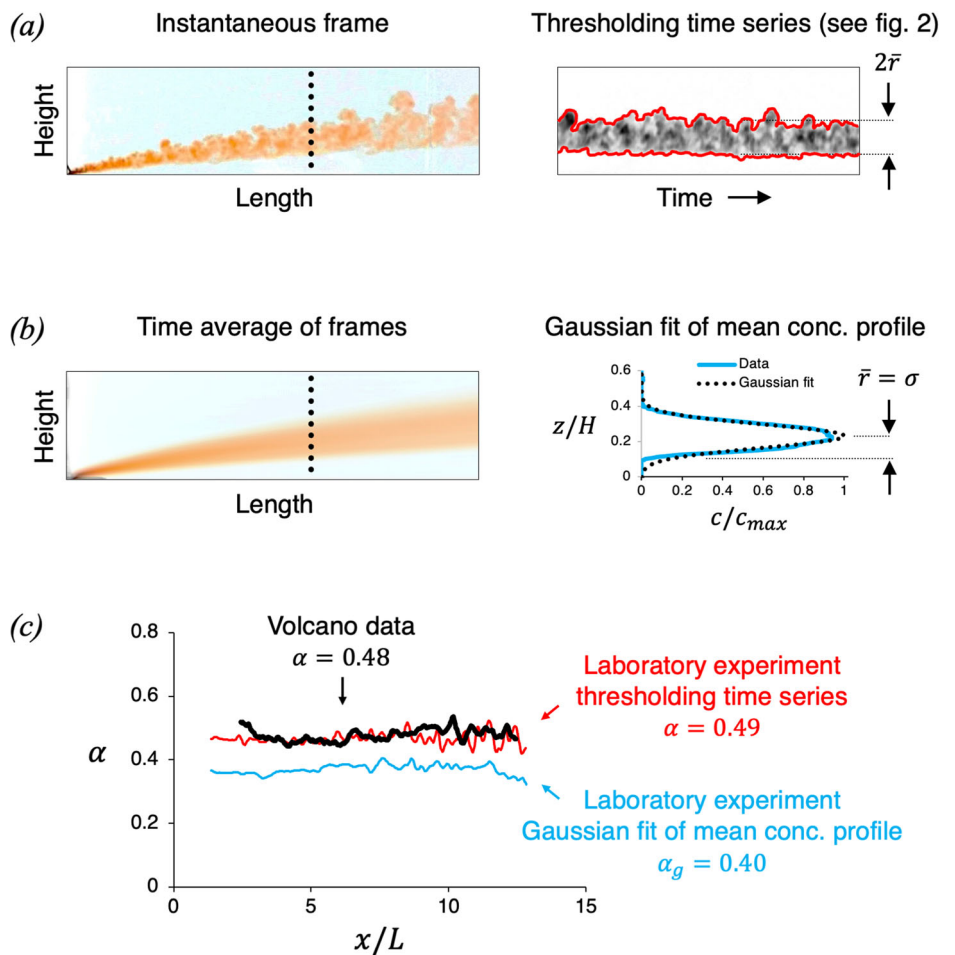


**Fig. 5 | Comparison of the entrainment coefficients  $\alpha$  in the eruption plume and in a laboratory plume.** **a** Using the same approach described in Fig. 2, we analyse each frame captured during a laboratory experiment and identify the edges of the plume, defined as the locus of points where the dye concentration is 1% of the maximum. We then estimate the instantaneous height and radius of the plume,  $z_c(x, t)$  and  $r(x, t)$  respectively, and use these estimates to quantify the associated time-averaged properties,  $\bar{z}_c(x)$  and  $\bar{r}(x)$ . Using this approach, we calculate  $\alpha = 0.49 \pm 0.03$  (see red line in panel c). **b** In laboratory plumes, the dye concentration field is known, and this enables us to use a different approach. We first calculate the time-averaged dye concentration field over the course of the experiment. At any given distance from the source,  $x$ , we then define the plume radius as the locus of points where the average dye concentration,  $c$ , is  $1/e$  of the maximum concentration,  $c_{max}$ <sup>16</sup>. Using this approach, we calculate  $\alpha_g = 0.40 \pm 0.05$  (see blue line in panel c). **c** Comparison of the values of  $\alpha$  as estimated from the eruption movie (thick black line) and from the laboratory movie. For the laboratory experiment, we plot two curves, which illustrate the different results obtained when using either of the two approaches above. On the horizontal axis, the distance from the source,  $x$ , is scaled by the length scale  $L = Bw^{-3}$  (see equation (2)).



concentration of dye varied according to a Gaussian away from the centreline of the plume. They then defined the radius  $r$  at each position in the plume to be the distance  $\sigma$  from the centreline at which the average concentration of dye in the plume fluid decays to factor  $1/e$  of the maximum concentration. For all the laboratory plumes analysed, they found  $\alpha_g = 0.40 \pm 0.05$  (see Fig. 5b and the blue line in Fig. 5c).

One difference between the volcanic plume and the laboratory plume is that the ash plume is nearly opaque, and so the boundary of the ash plume corresponds to the point where there is essentially no ash. In order to relate the laboratory experiments to the measurements from the ash plume, we have re-processed the experimental results presented in James et al.<sup>16</sup> (see Table 1), and defined the instantaneous edge of the laboratory plume to be

the point at which the concentration of dye is 1% of the maximum (Fig. 5a). Now the ratio of the plume radius to the centreline height  $r/z_c$  varies in time in a fashion directly equivalent to the volcanic plume, and has mean value  $\alpha = 0.49 \pm 0.03$  (red line in Fig. 5c). This is in good agreement with the estimate for  $\alpha$  for the wind-blown volcanic plume, suggesting the entrainment process is quantitatively similar.

**Comparison with a time-averaged model for a wind-blown plume: Plume shape and dynamics**

If the volcanic plume adjusts to the horizontal wind speed  $w$  relatively rapidly, then we can combine the equations of conservation of volume and momentum in the plume to obtain an expression for the plume

**Table 1 | Conditions of the laboratory experiments**

Exp	$Q \times 10^{-6}$	$g'$	$B \times 10^{-6}$	$w$
a	1.62	1.450	2.35	0.096
b	2.84	0.829	2.35	0.098
c	4.05	0.580	2.35	0.094
d	5.27	0.446	2.35	0.096
e	6.48	0.362	2.35	0.096
f	7.70	0.305	2.35	0.096
g	5.27	1.450	7.63	0.094
h	5.27	1.160	6.11	0.096
i	5.27	0.870	4.58	0.099
j	5.27	0.580	3.05	0.100
k	5.27	0.290	1.53	0.101
l	5.27	0.446	2.35	0.121
m	5.27	0.446	2.35	0.107
n	5.27	0.446	2.35	0.087
o	5.27	0.446	2.35	0.075
p	5.27	0.446	2.35	0.056
q	5.27	0.446	2.35	0.037

$Q$  ( $m^3 s^{-1}$ ) is the source volume flux;  $g'$  ( $m s^{-2}$ ) is the reduced gravity of the source fluid;  $B$  ( $m^4 s^{-3}$ ) is the source buoyancy flux; and  $w$  ( $m s^{-1}$ ) is the mean advection speed.

trajectory:<sup>13,16,17</sup>

$$x = \kappa L^{-\frac{1}{2}} z^{\frac{3}{2}} \tag{1}$$

where

$$L = Bw^{-3} \tag{2}$$

is the characteristic length scale for the wind-blown plume, given as a function of the time-averaged buoyancy flux  $B$ . Comparison of the model with laboratory data suggests that  $\kappa = 0.87 \pm 0.03$ <sup>16,18</sup> and indicates that the plume radius is given by

$$r(z) = \alpha z \tag{3}$$

In equation (1), we neglect the effects of ambient stratification, since at the downwind end of the field of view captured by the video, the plume is still rising, and has only reached a height of about 1.5 km.

We now compare the shape of the centreline of the ash plume with the predictions of the model. This allows us to assess the range of values of  $L$  which are consistent with the data. For each frame of the movie, we assess the difference between the model prediction and the data in terms of the fractional error

$$\varepsilon(L) = \frac{1}{x_{\max}} \int_0^{x_{\max}} \left( \frac{z_{c,model}(x, L)}{z_{c,data}(x)} - 1 \right)^2 dx \tag{4}$$

as a function of  $L$ .

In (Fig. 6a) we use a black dotted line to show the variation of this fractional error as a function of  $L$  using the time-average centreline  $z_c$  calculated for all the frames from the volcanic plume movie (see Fig. 4b). It is seen that the length scale which best fits the data is  $L = 204$  m. (Fig. 6a) also shows four coloured continuous lines, which illustrates how  $\varepsilon$  varies as a function of  $L$  when different portions of the movie are processed separately. It is seen that the best fitting values of  $L$  decrease over time during the eruption.

For comparison, in (Fig. 6b) we illustrate the results of a similar analysis which we have carried out using a video captured during a typical laboratory experiment (experiment b, see Table 1) in which a turbulent plume of fresh dyed water was released from a moving source into a tank 2.45 m long and which contained an aqueous saline solution<sup>cf. 16</sup>. In this case, the source condition  $L_{exp} = B_{exp}/w_{exp}^3$  was known. We have estimated the average shape of the plume, and then quantified  $\varepsilon$  for a range of values of  $L/L_{exp}$ . (Fig. 6b) shows that the minimum error  $\varepsilon_{min}$ , occurs for  $L = 0.985L_{exp}$ . Owing to the controlled conditions in the laboratory, the minimum error  $\varepsilon_{min}$  in (Fig. 6b) is slightly smaller than that obtained when processing the volcanic plume (Fig. 6a).

In order to explore the decrease in  $L$  with time suggested in (Fig. 6a), in (Fig. 7a, b) we illustrate how the best fit value of  $L$  varies over time during the 17 minutes-long recording of the volcanic eruption. For each frame in the eruption movie, we find the value of  $L$  which minimises the difference between the instantaneous shape of the ash plume and the theoretical shape given by equation (1). The blue lines in (Fig. 7a, b) show how this best-fit value of  $L$  and the associated error  $\varepsilon_{min}$  vary over time, which is plotted in dimensionless form using the time scale  $T = L/w = Bw^{-4}$ . In order to smooth out some of the turbulent fluctuations, we have also repeated our calculations using a rolling average of the centreline shape of the plume rather than the instantaneous shape, averaging over 2500, 5000, 7500 and 10,000 frames (coloured lines in Fig. 7a, b). It is seen that the misfit  $\varepsilon_{min}$  reduces significantly with the rolling average, as expected, but the estimate for  $L$  remains very similar. The data point to the observation that there is a gradual decrease in  $L$  during the eruption, from  $L \approx 296$  m to  $L \approx 168$  m, and since the wind field appears to be steady (see Fig. 1d), we infer that this relates to a gradual decrease in the eruption rate.

For comparison and calibration, (Fig. 7c, d) illustrate the results of a similar analysis of the frames captured during a typical laboratory experiment (experiment p in Table 1). Here, the best-fit estimate of  $L$  is essentially constant over time, and very close to the real value  $L_{exp}$  used in the experiment. The misfit  $\varepsilon_{min}$  tends to be smaller in the laboratory. A rolling average of the centreline shape of the plume reduces the impact of the turbulent fluctuations and therefore leads to smaller errors.

**Comparison of the adjustment process of a volcanic plume and a laboratory plume to the background flow speed**

Although the eruption rate appears to slowly decrease during the eruption, using the model prediction for the time-averaged buoyancy flux  $B$  we can examine whether the initial acceleration of the plume to the wind speed in the Eyjafjallajökull plume occurs over a similar dimensionless scale as the plumes in our laboratory experiments.

Figure 8a illustrates a time-averaged image of the volcanic plume. A number of coloured symbols have been superimposed onto this image, and indicate the positions at which the horizontal speed of the plume structures were measured from the movie as explained earlier. The speed was measured at a number of different heights, ranging from 225 to 1668 m above the vent, and downwind horizontal distances, ranging between 400 and 3650 m from the vent (see Fig. 8a). (Figure 8c) illustrates the results of our measurements. In order to compare these with our laboratory data, the results are plotted in dimensionless form, with the speed of the plume structures being scaled by the wind speed,  $u/w$ , and the height and length being given by  $z/L$  and  $x/L$ .

For comparison, we have analysed the frames captured during a series of laboratory experiments<sup>16</sup>. A time-averaged image of a laboratory saline plume is shown in (Fig. 8b). Again, the horizontal component of the speed of the plume,  $u$ , has been measured at several heights,  $z$ , and horizontal distances from the plume source,  $x$  (coloured symbols in Fig. 8b). Figure 8d illustrates the results of our measurements, plotted using the same scaling  $u/w$  and  $z/L$ , where in the laboratory  $w$  is the speed of the moving source. We observe that the volcanic and the laboratory plumes have a very similar

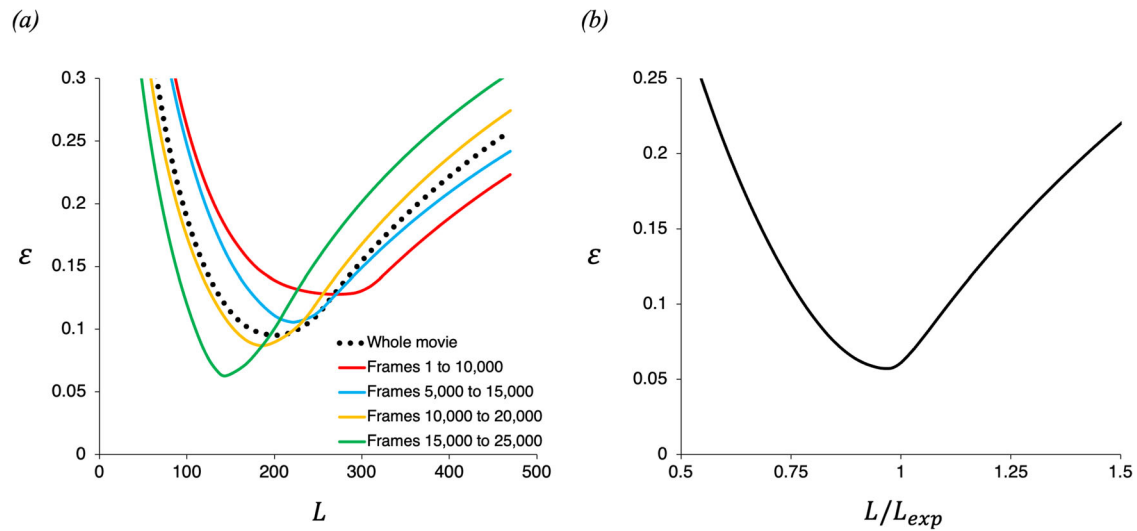


**Fig. 6 | Estimate of the difference  $\epsilon$  between the actual shape of the plume and the model prediction, as a function of the length scale  $L$ .** **a** Estimates of  $\epsilon$  (equation (4)), obtained while processing the eruption movie, for a range of values of the length scale  $L = Bw^{-3}$  (m). In plotting the black dotted line, we consider the mean trajectory of the plume as obtained by averaging all frames in the movie. In plotting the

coloured lines, we consider different portions of the movie separately. **b** For comparison, we estimate the difference  $\epsilon$  between the model prediction and the time-averaged shape of an experimental plume (experiment b in Table 1), for a range of values of  $L/L_{exp}$ , where the source condition  $L_{exp} = B_{exp}/w_{exp}^3$  is known (see Table 1).

pattern of adjustment to the wind speed, further supporting the similarity of the dynamics.

### Conversion of buoyancy flux to mass flux

In order to convert the length scale  $L = Bw^{-3}$  to an estimate for the mass flux associated with the eruption, we model the plume as being equivalent to a hot air plume of the same heat flux,

$$\rho_m Q_m c_{p_m} \Delta T_m = \rho_a Q_a c_{p_a} \Delta T_a \quad (5)$$

where  $\rho$  is density,  $Q$  is the volume flux,  $c_p$  is the heat capacity and  $\Delta T$  is the temperature difference, and where subscripts  $m$  and  $a$  denote ash and air respectively. The buoyancy flux of this hot air plume is

$$B = Q_a \frac{\Delta T_a}{T} g = Q_m \frac{\rho_m \Delta T_m c_{p_m}}{\rho_a T c_{p_a}} g \quad (6)$$

so that the volcanic mass eruption rate is approximately

$$\rho_m Q_m = \frac{T c_{p_a} \rho_a B}{\Delta T_m c_{p_m} g} \quad (7)$$

This result, combined with the assumption that  $\Delta T_m \approx 800$  °C, suggests that  $\rho_m Q_m \approx 0.0375B$ . With the wind speed  $w$  being of order  $w \approx 10$  m s<sup>-1</sup> (Fig. 1), we then estimate an initial mass eruption rate  $\rho_m Q_m \approx 1.11 \times 10^4$  kg s<sup>-1</sup>. However, as the eruption proceeds, this falls to about  $0.63 \times 10^4$  kg s<sup>-1</sup> (see Fig. 7a).

### Discussion

We have analysed data in a movie of a wind-blown volcanic plume, captured during the 2010 Eyjafjallajökull eruption, and compared them to carefully controlled laboratory experiments. We have found that the rate of mixing of air into the ash plume is comparable to that in the well-characterised laboratory plume, with entrainment coefficient  $\alpha \approx 0.4$ . Also, the shape of the time-averaged plume is in good agreement with the prediction of a simplified model of a buoyant plume in a cross-flow, and this enables us to estimate the buoyancy flux of the plume given an estimate of the wind speed. The non-dimensional length scale over which the ash plume adjusts to the wind speed is very similar to that of a laboratory plume, and this supports the

case that the laboratory plumes are dynamically similar to the large scale volcanic flow.

In comparing the eruption with the simplified plume model, we estimate that over the course of the 17 minutes-long recording, the eruption rate decreases from  $1.11 \times 10^4$  to  $0.63 \times 10^4$  kg s<sup>-1</sup>. The magnitude of the eruption rate we have estimated from the movie is consistent with the estimate by Gudmundsson et al.<sup>19</sup>, who reported magma discharge rates of order  $10^4$  kg s<sup>-1</sup> on the day the movie was recorded.

The approach described in this paper opens the way to estimate eruption rates from video recordings of explosive eruptions. Our modelling approach applies to eruptions in which the flow rate is sufficiently small that the plume is wind-blown. This requires the wind speed  $w$  to exceed the plume speed,  $u$ . Woitischek et al.<sup>18</sup> showed that the wind-blown plume speed is given by

$$u = \gamma \left( \frac{B}{w} \right)^{\frac{1}{2}} z^{-\frac{1}{2}} \quad (8)$$

where  $\gamma = 0.57$  is a dimensionless constant estimated using a series of laboratory experiments<sup>18</sup>. Using (8), we calculate that there is a critical height above the source,  $z^*$ , at which the plume speed equals the wind speed:

$$z^* = \gamma^2 \frac{B}{w^3} = \gamma^2 L \quad (9)$$

We expect the model introduced in this paper to apply for  $z \gg z^*$ , where the plume is strongly wind-blown. The data presented in this paper, obtained from the analysis of the video recording of the eruption, focus on the shape and dynamics of the plume at heights ranging between 400 and 1800 m (see Figs. 1c, 3 and 8). Using the predictions of the model based on this data, we estimate that the critical height  $z^* \approx 55$ –96 m (see Fig. 9). Since  $z^* \ll 400$  m, it follows that our analysis is consistent with the model.

In addition, the approach discussed in this paper assumes that the speed of wind is relatively uniform with height, and this is consistent with the observation of wind speed (Fig. 1c), which suggests that the vertical variation in the wind is less than 8%.

Finally, our modelling approach is based on the time-averaged plume shape as a function of distance from the source. This requires a video recording that is sufficiently long that it captures the passage of several

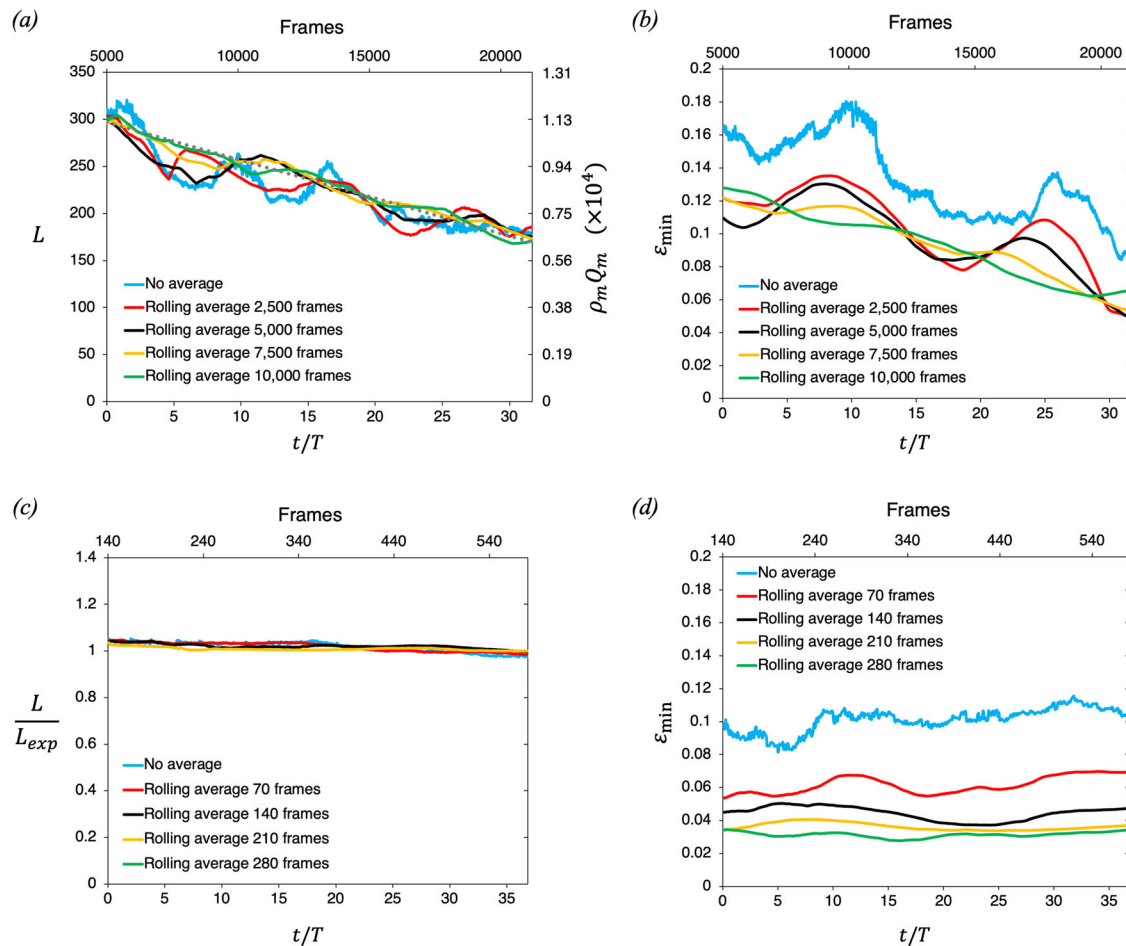


**Fig. 7 | Estimates of  $L$  and  $\epsilon$  over the course of the volcanic eruption and a typical laboratory experiment.** In panels (a, b) we focus on the volcano movie. For each frame in the movie, we estimate the instantaneous shape of the ash plume and compare it with the shape predicted by the model (equation (1)) for a range of values of  $L = B/w^3$ . For each frame, we identify the value of  $L$  which has the minimum error  $\epsilon_{min}$ , and use a blue line to plot how: (a) the instantaneous best-fit estimate of  $L$  and (b) the instantaneous minimum error  $\epsilon_{min}$  vary over time. On the horizontal axis, time  $t$  is scaled by the time scale  $T = B/w^3$ . We then repeat the same analysis for a series of rolling time averages of the plume shape (2500 frames red; 5000 black; 7500

yellow and 10,000 green). We observe that as we average over more frames the error decreases, but we find very similar estimates for  $L$ . Our data suggest that  $L$  decreases steadily over time during the 17 minutes-long movie of the eruption. On the secondary vertical axis in panel (a) we estimate the eruption rate,  $\rho_m Q_m$  (see section Conversion of buoyancy flux to mass flux). In panels (c, d) we carry out a similar analysis of a typical experiment movie (experiment p in Table 1). As expected, the best-fit estimate of  $L$  is now constant over the duration of the experiment and consistent with the true conditions of the experiment,  $L_{exp}$  (c), while the errors  $\epsilon$  are smaller in the controlled laboratory setting (d).

eddies through the field of view of the plume. Since the time scale of ascent of the plume scales as<sup>18</sup>

$$\frac{z}{u} = \frac{1}{\gamma} \left( \frac{B}{w} \right)^{-\frac{1}{2}} z^{\frac{3}{2}} \quad (10)$$

and given that the average size of the eddies in the wind-blown plume,  $\delta$ , scales with the plume height  $z$ <sup>16</sup>,

$$\frac{\delta}{z} = 0.84 \pm 0.10 \quad (11)$$

we estimate that the time for  $n$  eddies to pass through the field of view from height  $z = 0$  to height  $z = H$  (e.g., 400 m) is

$$\tau = 0.84 \frac{n}{\gamma} \left( \frac{B}{w} \right)^{-\frac{1}{2}} H^{\frac{3}{2}} \quad (12)$$

For  $5 < n < 10$ , this corresponds to  $340 < \tau < 680$  s, while the eruption movie that we have analysed is 1050 s long.

## Methods

We have presented data obtained from the analysis of a video recording of the eruption of the Eyjafjallajökull volcano in Iceland, and we have compared this data to a model which has been developed based on the results of a number of laboratory experiments<sup>16</sup>. The eruption movie contained approximately 26,200 frames (see Fig. 1a). Each frame was of a resolution  $1440 \times 810$  pixels in the RGB space, and was imported and processed individually using Matlab R2023a software.

Figure 1b shows how the speed of the wind and of the plume eddies were measured using the video recording of the eruption. For each frame in the video, we selected a horizontal line of pixels (denoted by a dotted line in Fig. 1a) and plotted a time series of this line of pixels in (Fig. 1b). Here, a number of descending inclined fronts are visible, and illustrate the motion of the plume eddies over time. Following Mingotti & Woods<sup>15</sup>, we used the Hough transform algorithm as available in Matlab to identify these fronts, calculate their gradient and thereby estimate the horizontal component of the plume speed as a function of the horizontal distance from the plume source,  $x$ , at a given height above the source,  $z$ . In order to plot the vertical speed profile shown in (Fig. 1c), we repeated this measurement using eight different time series images (such as the one shown in panel b), generated



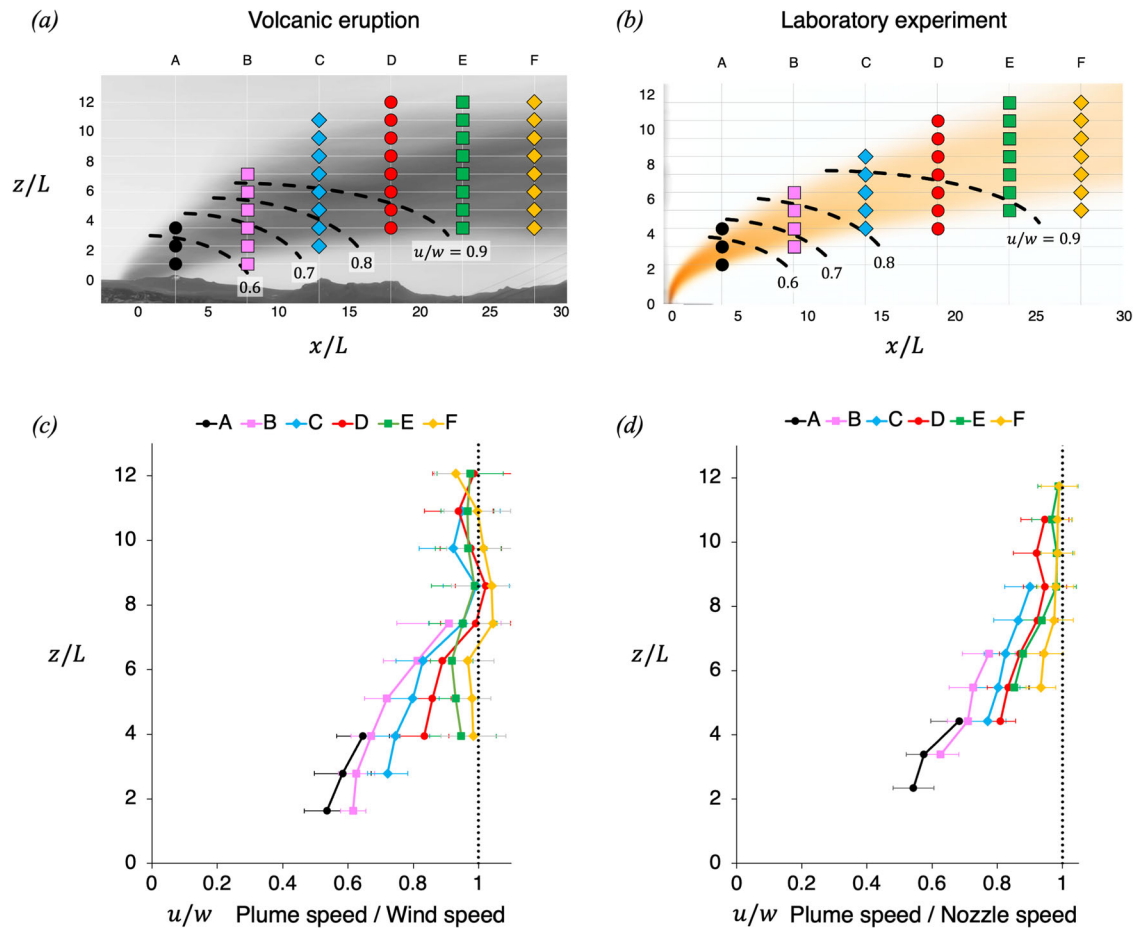


**Fig. 8 | Comparison of the adjustment processes of the volcanic plume and a laboratory plume to the background flow speed.** **a, b** Time-averaged images of (a) the volcanic plume and (b) a small-scale laboratory plume. In both panels, a grid of coloured symbols is used to indicate the different heights and horizontal distances from the plume source at which the plume speed is measured. **c** Horizontal speed of the volcanic ash plume,  $u$ , relative to the background wind speed,  $w$ , measured at a

number of points, as indicated in panel (a). **d** Horizontal speed of the laboratory plume fluid,  $u$ , relative to the ambient fluid speed in the frame of the moving nozzle,  $w$ , measured at a number of points, as indicated in panel (b). Error bars in panels (c, d) illustrate the standard deviation of the velocity measurements relative to the mean.

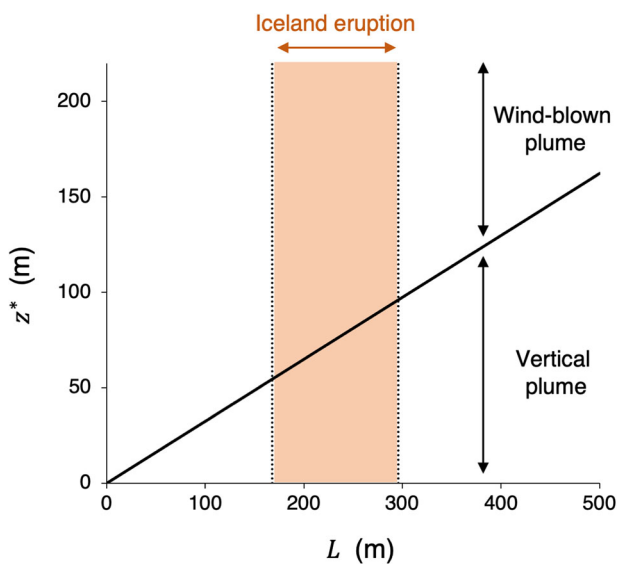


**Fig. 9 | Condition for the plume to be wind-blown.** We use equation (9) to estimate the critical height  $z^*$  above which the plume is wind-blown, as a function of the length scale  $L$ . The shaded area illustrates the range of values of  $L$  estimated for the Iceland eruption (see Fig. 7a).

using horizontal lines of pixels located at different heights above the source (see dotted line in panel a).

Figure 2 shows how the plume height and radius were measured. For each frame in the video, we selected a number of vertical lines of pixels and plotted a time series of each of these lines: (Fig. 2a–c) show three of these time series images, taken at different horizontal distances from the source. Each of these images was then processed independently. By focussing on the blue channel of each image, we could identify the pixels containing a grey hue and distinguish them from those containing a blue hue: this enabled us to identify and threshold the edges of the ash plume, and then estimate the location of the plume centreline, as discussed in Variation of the plume radius and height with distance from the vent.

Laboratory experiments were carried out in a Perspex tank of dimensions  $245 \times 60 \times 35$  cm: analogous laboratory experiments have been described by ref. 16. The tank was filled with fresh, stationary water, and was connected to a moving plume source. During an experiment, this source was moved at a controlled speed along the top of the tank. A peristaltic pump was used to supply saline, dyed fluid through the source nozzle, and this formed a negatively buoyant, turbulent plume which descended through the tank. By Lagrangian transformation, we expect this plume to be equivalent to the plume which develops when there is a stationary source of buoyant fluid in a uniformly translating body of ambient fluid<sup>[cf. 16]</sup>. The tank was backlit using a light panel which provided uniform illumination, and a

Nikon D5300 Full-HD 60 Hz camera was located on the opposite side to capture a video recording of each experiment.

The frames captured during the laboratory experiments were analysed using the same image analysis techniques as the frames from the eruption movie. Figure 5a shows an instantaneous frame captured during a typical laboratory experiment, and illustrates how the edges of the plume at a given horizontal distance from the source were identified by thresholding a time series of a vertical line of pixels, using the same approach discussed above. (Fig. 5b) illustrates an alternative method, based on the time-averaging of the plume frames. Following<sup>16</sup>, the size of the plume and the entrainment coefficient were then estimated using a Gaussian fitting of the time-averaged dye concentration profile, as discussed in Comparison with a time-averaged model for a wind-blown plume: Plume radius and entrainment coefficient. (Fig. 5c) shows that these two alternative approaches to estimating the plume entrainment coefficient provided consistent results.

### Data availability

The data sets presented in this article have been generated using the video of the Eyjafjallajökull eruption, which is available at this link: <https://doi.org/10.5281/zenodo.10842769>.

Received: 22 November 2023; Accepted: 18 April 2024;

Published online: 07 May 2024

### References

1. Sparks, R. S. J. The dimensions and dynamics of volcanic eruption columns. *Bull. Volcanol.* **48**, 3–15 (1986).
2. Woods, A. W. The fluid dynamics and thermodynamics of eruption columns. *Bull. Volcanol.* **50**, 169–193 (1988).
3. Sparks, R. S. J. et al. *Volcanic plumes* (John Wiley & Sons, Inc, United States, 1997).
4. Morton, B. R., Taylor, G. I. & Turner, J. S. Turbulent gravitational convection from maintained and instantaneous sources. *Proc. Royal Soc. London. Ser. A. Math. Phys. Sci.* **234**, 1–23 (1956).
5. Carazzo, G. & Jellinek, A. M. A new view of the dynamics, stability and longevity of volcanic clouds. *Earth Planetary Sci. Lett.* **325–326**, 39–51 (2012).
6. Carazzo, G., Girault, F., Aubry, T., Bouquerel, H. & Kaminski, E. Laboratory experiments of forced plumes in a density-stratified crossflow and implications for volcanic plumes. *Geophys. Res. Lett.* **41**, 8759–8766 (2014).
7. Carazzo, G., Kaminski, E. & Tait, S. The timing and intensity of column collapse during explosive volcanic eruptions. *Earth Planetary Sci. Lett.* **411**, 208–217 (2015).
8. Devenish, B. J., Rooney, G. G., Webster, H. N. & Thomson, D. J. The entrainment rate for buoyant plumes in a crossflow. *Boundary-Layer Meteorol.* **134**, 411–439 (2010).
9. Woodhouse, M. J., Hogg, A. J., Phillips, J. C. & Sparks, R. S. J. Interaction between volcanic plumes and wind during the 2010 eyjafjallajökull eruption, iceland. *J. Geophys. Res.: Solid Earth* **118**, 92–109 (2013).
10. Dellino, P. et al. Volcanic jets, plumes, and collapsing fountains: evidence from large-scale experiments, with particular emphasis on the entrainment rate. *Bull. Volcanol.* **76**, 1–18 (2014).
11. Aubry, T. J. & Jellinek, A. M. New insights on entrainment and condensation in volcanic plumes: Constraints from independent observations of explosive eruptions and implications for assessing their impacts. *Earth Planetary Sci. Lett.* **490**, 132–142 (2018).
12. Hoult, D. P., Fay, J. A. & Forney, L. J. A theory of plume rise compared with field observations. *J. Air Poll. Control Asso.* **19**, 585–590 (1969).
13. Hewett, T. A., Fay, J. A. & Hoult, D. P. Laboratory experiments of smokestack plumes in a stable atmosphere. *Atmosph. Environ.* **5**, 767–789 (1971).
14. Manzella, I., Bonadonna, C., Phillips, J. C. & Monnard, H. The role of gravitational instabilities in deposition of volcanic ash. *Geology* **43**, 211–214 (2015).
15. Mingotti, N. & Woods, A. W. On turbulent particle fountains. *J. Fluid Mech.* **793**, 1–12 (2016).
16. James, C. B. G., Mingotti, N. & Woods, A. W. On particle separation from turbulent particle plumes in a cross-flow. *J. Fluid Mech.* **932**, A45 (2022).
17. Chu, V. H. Turbulent dense plumes in a laminar cross flow. *J. Hydraulic Res.* **13**, 263–279 (1975).
18. Woitischek, J., Mingotti, N., Edmonds, M. & Woods, A. W. On the use of plume models to estimate the flux in volcanic gas plumes. *Nat. Commun.* **12**, 1–8 (2021).
19. Gudmundsson, M. T. et al. Ash generation and distribution from the april-may 2010 eruption of eyjafjallajökull, iceland. *Sci. Rep.* **2**, 1–12 (2012).

### Acknowledgements

The authors wish to thank professor Costanza Bonadonna of Geneva University for providing the eruption video.

### Author contributions

A.W.W. initiated and supervised the research. N.M. carried out the laboratory experiments. Both authors contributed to the analysis of the data and the writing of the article.

### Competing interests

All authors declare no competing interests.

### Ethical approval

The authors support inclusive, diverse, and equitable conduct of research.

### Additional information

**Supplementary information** The online version contains supplementary material available at <https://doi.org/10.1038/s43247-024-01402-x>.

**Correspondence** and requests for materials should be addressed to Andrew W. Woods.

**Peer review information** *Communications Earth & Environment* thanks Valentin Freret-Lorgeril and the other, anonymous, reviewer(s) for their contribution to the peer review of this work. Primary Handling Editors: Domenico Doronzo and Joe Aslin. A peer review file is available.

**Reprints and permissions information** is available at <http://www.nature.com/reprints>

**Publisher's note** Springer Nature remains neutral with regard to jurisdictional claims in published maps and institutional affiliations.

**Open Access** This article is licensed under a Creative Commons Attribution 4.0 International License, which permits use, sharing, adaptation, distribution and reproduction in any medium or format, as long as you give appropriate credit to the original author(s) and the source, provide a link to the Creative Commons licence, and indicate if changes were made. The images or other third party material in this article are included in the article's Creative Commons licence, unless indicated otherwise in a credit line to the material. If material is not included in the article's Creative Commons licence and your intended use is not permitted by statutory regulation or exceeds the permitted use, you will need to obtain permission directly from the copyright holder. To view a copy of this licence, visit <http://creativecommons.org/licenses/by/4.0/>.

© The Author(s) 2024